Supplementary information to the manuscript "*Tunable strain and bandgap in subcritical-sized MoS_2 nanobubbles*"

Michele Gastaldo,[*,†] Javier Varillas,[*,‡,†] Álvaro Rodríguez,[†,⁋] Matěj Velický,[†] Otakar Frank,[†] and Martin Kalbáč[*,†]

[†] J. Heyrovský Institute of Physical Chemistry, Czech Academy of Sciences, Dolejškova 2155/3, 182 23 Prague, Czech Republic

[‡] Institute of Thermomechanics, Czech Academy of Sciences, Dolejškova 1402/5, 182 00 Prague 8, Czech Republic

[⁋] Materials Science Factory, Instituto de Ciencia de Materiales de Madrid, Consejo Superior de Investigaciones Científicas, 28049 Madrid, Spain

[*] **E-mail addresses:** michele.gastaldo@jh-inst.cas.cz; jvarillas@it.cas.cz; martin.kalbac@jh-inst.cas.cz

S1. Bias-dependent apparent height of MoS_2 nanobubbles

The heights measured by STM can differ from the real heights because the *z*-movement of the tip is controlled by the tunneling current. This is a measurement of the density of states of the sample (integrated from energy 0 to eV_{bias}, where V_{bias} is the bias voltage applied and e is the electron charge), and thus it depends on the local electronic properties of the surface in addition to the topographic ones. As a result, not only the relative heights of different features on the measured surface can be misrepresented (for instance, an adsorbate might appear lower than its surroundings; see, e.g., Ref. [3]), but also the height of a single feature might differ at different bias voltages (as is the case for the moiré pattern of MoS_2/Au(111) [4]). This is because topographic scans are typically acquired in constant current mode, and new (or fewer) tunneling channels might be available with different V_{bias}. For this reason, the height measured by STM is typically referred to as *apparent height* and is usually verified by other measurements (e.g., AFM).

The apparent-height issue was relevant when assessing the aspect ratio of our MoS_2 nanobubbles. To avoid misinterpretations, not only we have confirmed the h/R ratio by AFM measurements (Fig. 1(d) of the main text), but also we have verified the bias dependency of the height measured in our STM experiments. In this regard, Fig. S1(a) shows the bias-dependent measurements of the height of two bubbles with different radii: Bubble 1 with $R = 8.1$ nm and Bubble 2 with $R = 14.0$ nm. We found that the apparent height ranges between 0.7 and 1.1 nm for Bubble 1 and between 2.8 and 3.2 nm for Bubble 2. Thus, a height difference of up to 50% can arise on a bubble if the bias voltage is not constant. However, it is observed in this simple analysis that when V_{bias} ranges between 1 and 1.5 V the bubble's height is constant within a maximum error of 10%. To ensure consistency in our h/R measurements, we then selected this V_{bias} range to acquire topographic scans of the MoS_2 nanobubbles.

We note that also the measurement of the radius is V_{bias} -dependent. Comparing scans at positive and negative polarity (Figs. S1(c, d), respectively), we observe that a dip seems to appear at the edge of nanobubbles when $V_{\mathrm{bias}} < 0$, whereas at positive bias the membrane falls smoothly onto the terrace; see Fig. S1(b). This behavior might be caused by the presence of bound states at the edge of nanobubbles, similar to those observed in $WSe_2/MoSe_2$ heterobilayers [4], which results in different topographic appearances at different V_{bias}. However, the concurrent decrease of h and R at negative polarities with respect to positive ones results in the same h/R value (with <1% error). Thus, the bias dependence of the h/R evolution with R appears to be negligible.

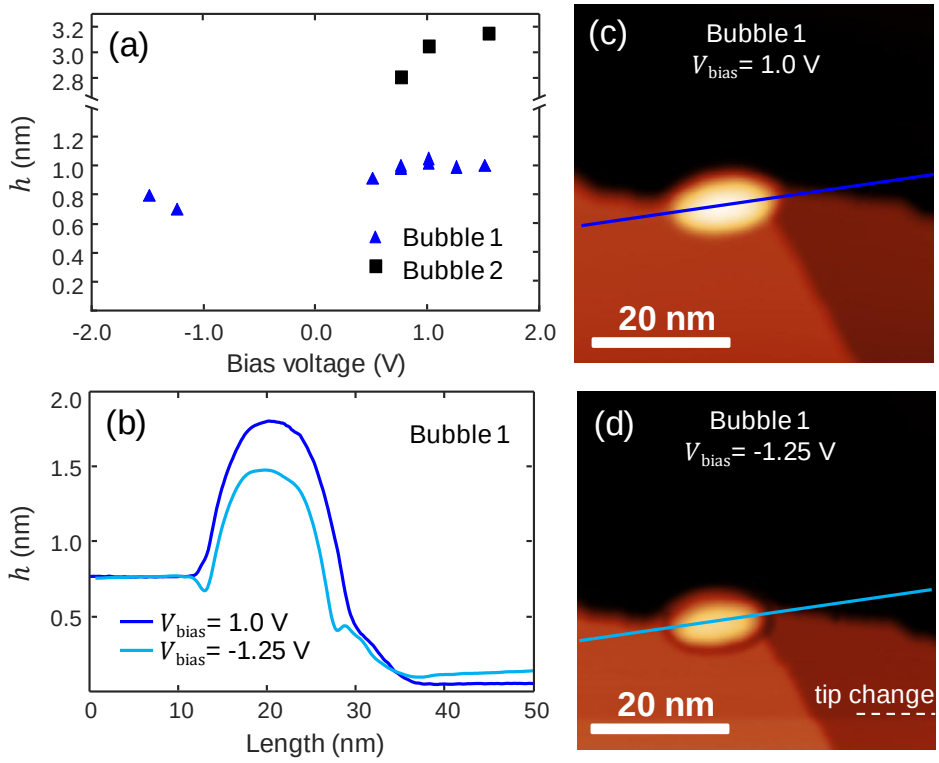

Figure S1. Bias dependency in STM measurements of height and radius of nanobubbles. (a) Height measurements as a function of the bias voltage, V_{bias}. (b) Profiles of Bubble 1 (marked in (c) and (d)) as a function of V_{bias}. A STM tip apex change is observed in the bottom of (d); however, the height measurement was reproducible afterward. STM topographic scans of a bubble with $R = 8.1$ nm at (c) $V_{\mathrm{bias}} = 1.0$ V and (d) $V_{\mathrm{bias}} = -1.25$ V. The setpoint current was set to $I_{\mathrm{t}} = 0.2$ nA.

S2. Profile fitting of MoS_2 nanobubbles

We approximate our MD and STM profiles of MoS_2 nanobubbles to the analytical model proposed by Blundo et al. [20] by using the least squares approach. To this end, we adopt the fitting curve

$$z(x) = h\left[1 - \left(\frac{x - x_0}{R}\right)^q\right], \tag{S1}$$

where h, x_0, R, and q are the 4 free parameters; see Fig. S2.

The results given in Table S1 follow a decent agreement with those by Blundo et al. (cf. Fig. 2(b) in Ref. [20]) in large MoS_2 bubbles with fixed h/R at ≈0.22 where $q \approx 2.2$. For smaller MoS_2 bubbles ($R < R_{\mathrm{c}}$), we find in our fitting results a reduction in the exponent q, where $q < 2$.

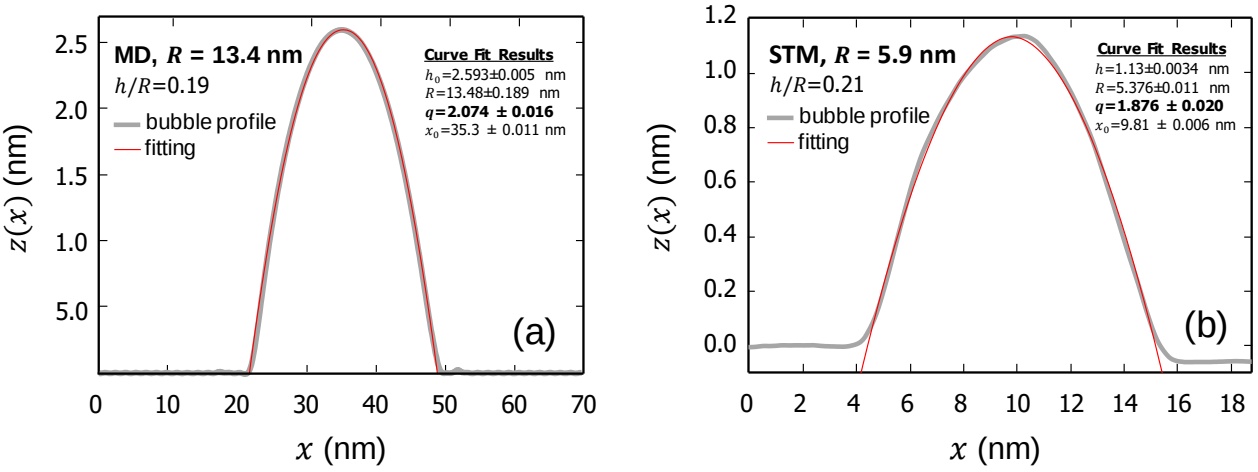

Figure S2. Fitting of the MoS_2 nanobubble profiles adopting Eq. (S1). (a) MD bubble of $R = 13.4$ nm and (b) experimental bubble of $R = 5.9$ nm measured by STM.

Table S1. Values of the fitted exponent q from the STM and MD profiles of MoS_2 nanobubbles.

STM measurements			MD simulations		
R (nm)	h/R	q	R (nm)	h/R	q
2.1	0.13	1.83	6.7	0.13	1.65
3.4	0.16	2.0	7.3	0.14	1.66
5.9	0.20	1.88	8.9	0.14	1.88
6.6	0.16	2.26	11.6	0.16	1.93
7.3	0.20	1.91	13.4	0.19	2.07
9.6	0.20	2.26	21.0	0.21	2.16
24.4	0.23	2.32	26.4	0.20	2.19

S3. MD cells containing the MoS_2/Au(111) system with trapped atoms

We construct the periodic MoS_2/Au(111) system by placing a MoS_2 membrane on top of a flat, (111)-oriented Au substrate comprised of two rigid atomic layers. The x-direction follows the armchair orientation of the MoS_2 membrane. The atoms are initially located at their equilibrium distance satisfying the lattice parameters predicated by the interatomic potentials. The initial MoS_2-substrate separation is defined in accord with the equilibrium interlayer distance prescribed by the interlayer potentials (Section S6).

Then, we modify the z coordinates of the constituent atoms in the MoS_2 membrane using the equation of a bell shape,

$$z = z_0 + h_0 \exp\left(\frac{(x - l_x/2)^2 + \left(y - l_y/2\right)^2}{\beta}\right), \quad \text{(S2)}$$

where l_x and l_y represent the dimensions of the MoS_2/Au(111) system (Fig. S3(a)), h_0 is the height of the bell (Fig. S3(b)), and β is a fitting parameter. The x and y coordinates remain unchanged. This creates a space between the membrane and the substrate in which trapped N atoms are inserted at random positions; see the red-marked region in Fig. S3(b).

The number of N atoms, N_{N}, to be introduced is approximated considering the ideal gas law which stipulates that $N_{\mathrm{N}} = (N_{\mathrm{Av}}\, \rho_{\mathrm{N}}\, V_{b,0})/W_{\mathrm{N}}$; where N_{Av} is the Avogadro's number, ρ_{N} stands for the density of nitrogen gas ($\rho_{\mathrm{N}} = 1250.6\ \mathrm{g/cm^3}$ at atmospheric pressure), $V_{\mathrm{b},0}$ is the initial bubble's volume defined by a hemisphere of radius r (note that $r < h$; see Fig.S3(b)), and W_{N} accounts for the standard atomic weight of N.

This computational method was envisioned to reproduce the experimental conditions that allow trapped atoms−between the membrane and the substrate− to form nanosized bubbles during exfoliation (see Experimental Methods in the main text). In Table S2, we provide the details of all the as-built MD cells considered for this investigation, including the parameters that define the initial bell-shaped MoS_2 membranes and $V_{b,0}$.

Table S2. Details of the (16) MoS_2/Au(111) systems with trapped N atoms simulated for this study.

MoS_2/Au(111) size	*# MoS_2 atoms*	*# Au atoms*	*# N atoms*	*h_0 (nm)*	*r (nm)*	*β (nm²)*	*R (nm)*
10×10 nm	3,456	2,499	66	1.3	1.05	6	2.4
15×15 nm	7,776	5,624	362	2.0	1.8	13	3.9
20×20 nm	13,392	9,506	788	2.5	2.25	25	5.4
25×25 nm	21,060	14,884	1,112	2.8	2.5	35	5.8
25×25 nm	21,060	14,884	1,602	3.1	2.8	35	6.3
25×25 nm	21,060	14,884	1,993	3.3	3.0	35	6.7
30×30 nm	30,456	21,756	1,594	3.1	2.8	50	7.3
40×40 nm	54,432	38,808	3,685	4.0	3.6	100	8.9
50×50 nm	84,240	59,536	9,349	5.1	4.8	150	11.6
70×70 nm	167,640	118,680	19,116	6.4	6.0	180	13.4
70×70 nm	167,640	118,680	19,120	7.0	6.7	200	14.0
85×85 nm	245,784	173,888	34,285	7.6	7.2	225	16.6
100×100 nm	341,004	241,572	40,688	8.0	7.6	250	17.2
115×115 nm	449,280	317,532	79,521	9.8	9.4	400	21.0
130×130 nm	575,280	407,043	112,543	11.0	10.5	500	26.4
140×140 nm	664,884	469,910	199,110	13.0	12.6	800	31.8

Figures S3(a, b) show the as-built 20-by-20-nm MoS_2/Au(111) system containing trapped atoms between the bell-shaped MoS_2 and the Au substrate. The relaxed MoS_2/Au(111) system containing a thermodynamically stable nanobubble is given in Fig. S3(e). The time evolution of the bubble's temperature (T_b) and pressure (P) during the relaxation run are plotted in Figs. S3(c, d), respectively. Note that thermodynamical equilibrium is attained when dT_b/dt and dP/dt fluctuates around 0.

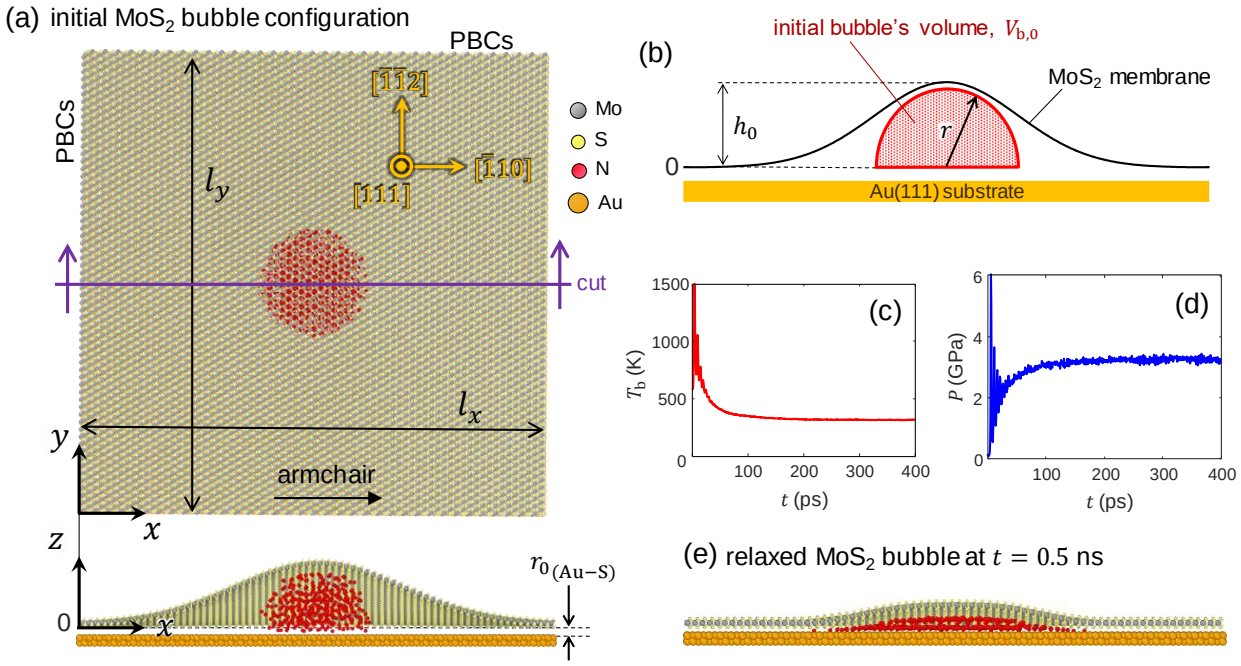

Figure S3. The computational domain with periodic boundary conditions (PBCs). (a) Top view and front (cut marked with the purple line) view of the as-built 20×20-nm MD cell comprised of a top, bell-shaped MoS_2 and a bottom, (111)-oriented Au substrate between which N atoms are introduced (inside $V_{b,0}$, cf. part (b)). The yellow arrows denote the crystalline orientation of the main axes in the Au substrate. (b) Schematic representation of the as-built MD configuration. (c, d): Time evolution of temperature, T_b, and hydrostatic pressure, P, of the trapped atoms during the relaxation of the MoS_2/Au(111) heterosystem. (e) Cross-sectional cut of the relaxed system containing a MoS_2 nanobubble of radius R=5.4 nm.

S4. MoS_2 nanobubbles formed on substrate steps

While the MD simulations discussed in the main text consider MoS_2 bubbles formed on perfectly flat Au(111) substrates (Section S3), a considerable number of the experimental nanobubbles evaluated in this investigation were formed at the rim of Au terraces characterized by monoatomic and biatomic steps. Bearing this in mind, we discuss in the following the general influence that such Au steps have on the relaxed shape of MoS_2 nanobubbles. To do so, we present a comparative

analysis of MoS_2 bubbles with $R \approx 17$ nm formed at the edge of Au steps against those formed on a flat Au(111) substrate. Note that $R > R_c$.

We separately create two periodic Au (111) substrates that contain a longitudinal step along x characterized by a monoatomic and biatomic step height (note that, in an Au crystal, one atomic spacing along the [111] direction has magnitude $a\sqrt{3}/3 \approx 0.23$ nm; cf. Fig. S6(a)). The MoS_2 bubbles are then relaxed following the computational method described in the main text and in Section S3 using 100x100-nm periodic cells. The location of the steps in our MD cells ensures that the rim of the relaxed bubbles marginally overpasses the Au terrace, as illustrated in Figs. S4(b, c). Such a configuration of MoS_2 nanobubbles formed at terrace edges aims to mimic those found in our STM topographies from our MoS_2/Au(111) experiments; compare, e.g., Fig.1(b) in the main text with Fig. S5(a, b).

The profiles plotted in Fig.S4(d) show that MoS_2 nanobubbles formed at the edge of Au terraces tend to marginally increase R and decrease h as compared to those formed on perfectly flat Au (111) substrates. Because R is measured along the major axis, the h/R value consequently varies from $h/R \approx 0.22$ (flat Au substrate) to $h/R \approx 0.20$ when biatomic steps are incorporated into the MD cells. Table S3 provides the characteristic sizes measured in relaxed MoS_2 nanobubbles obtained under the three distinct substrate configurations; see Figs. S4(a-c). Notice in these figures that the Au substrates (under the MoS_2 bubble) are composed of two (111)-oriented Au planes so that the adhesion energy between the MoS_2 and the Au substrate remains roughly the same under all of the substrate configurations.

The MoS_2 topographies shown in Figs. S5(a-c) illustrate the effect of Au steps on the relaxed nanobubble shapes. It is found that MoS_2 nanobubbles located at the rim of substrate steps tend to develop topographies with a lenticular shape (in top view)−compare Figs. S5(a, c). On this note, we calculate the projected aspect ratio of the relaxed nanobubbles (that is the ratio between the minor axis and the major axis as measured in the projected bubble's area), which varies from ≈ 0.98 (flat Au substrate) to ≈ 0.82 under Au terraces with a biatomic step. These results quantify the effective variation in the relaxed bubble shapes obtained under these different conditions.

On the other hand, the local strain maps shown in Figs. S5(d-f) display the role that the presence of terrace steps has in the resulting local strain distributions of MoS_2 nanobubbles. Interestingly, the bubble's volume takes similar values under the three distinct substrate configurations ($V_b \approx 1{,}100$ nm^3), thus indicating that the evolution from circular- to lenticular-shaped MoS_2 nanobubbles (see Figs. S5(a-c), respectively) relates to an overall built-up in atomic-level stresses. This, in turn, provokes an additional increase in the pressure (P) inside the nanobubbles; see Table S3. By contrast, the MoS_2 bubbles exhibit a mild reduction in the average

local strains ($\varepsilon_{\text{bubble}}$) when it comes to nanobubbles formed at the edge of Au steps; see also Table S3.

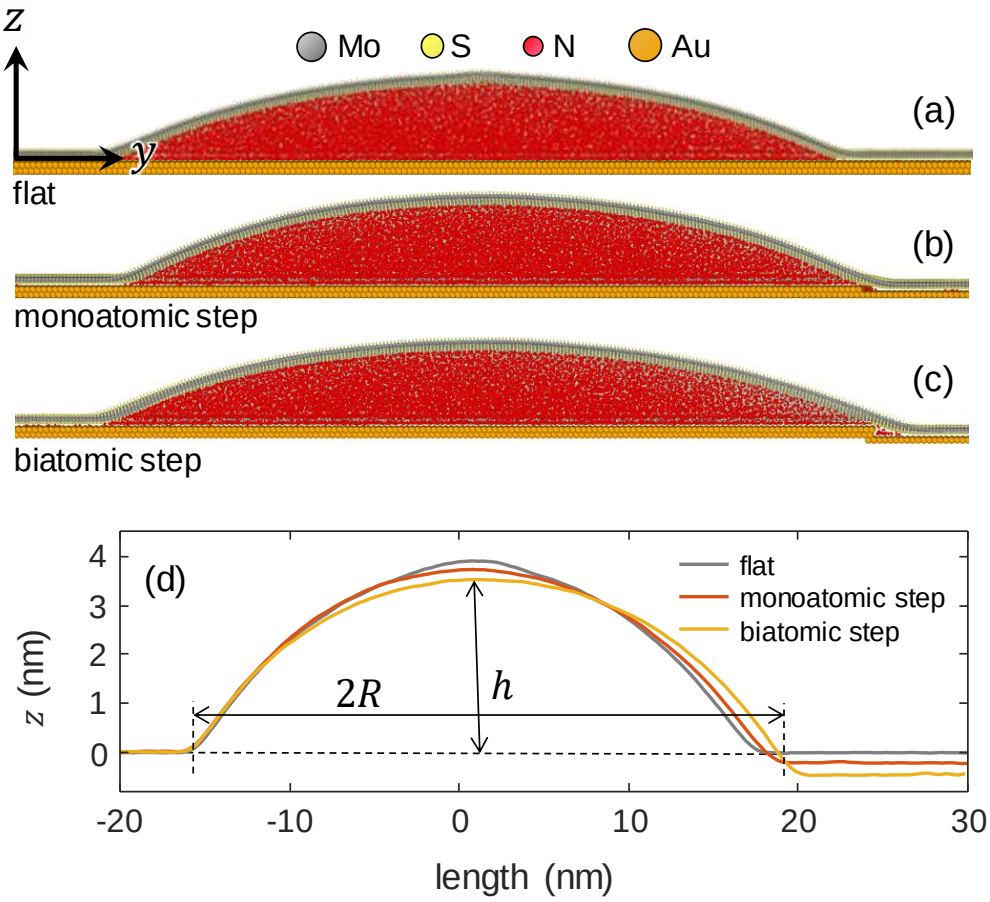

Figure S4. Cross-section cuts of relaxed MoS_2 nanobubbles ($R \approx 17$ nm) in 100×100-nm periodic MD cells with a flat Au (111) substrate (a), a substrate with a monoatomic step (b), and a substrate with a biatomic step (c). The respective bubble profiles are given in (d). The h and $2R$ distances marked in (c) refer to the MoS_2 bubble formed on a substrate with a biatomic step. The profile cuts are marked in green in the MoS_2 topographies from Figs. S5(a-c).

Table S3. Bubble properties obtained from 100x100-nm MD cells as a function of substrate topography.

substrate configuration	h (nm)	R (nm)	h/R	P (MPa)	$\varepsilon_{\text{bubble}}$ (%)
flat	3.7	16.8	0.22	335	6.65
monoatomic step	3.6	16.9	0.21	350	6.43
biatomic step	3.5	17.3	0.20	370	6.34

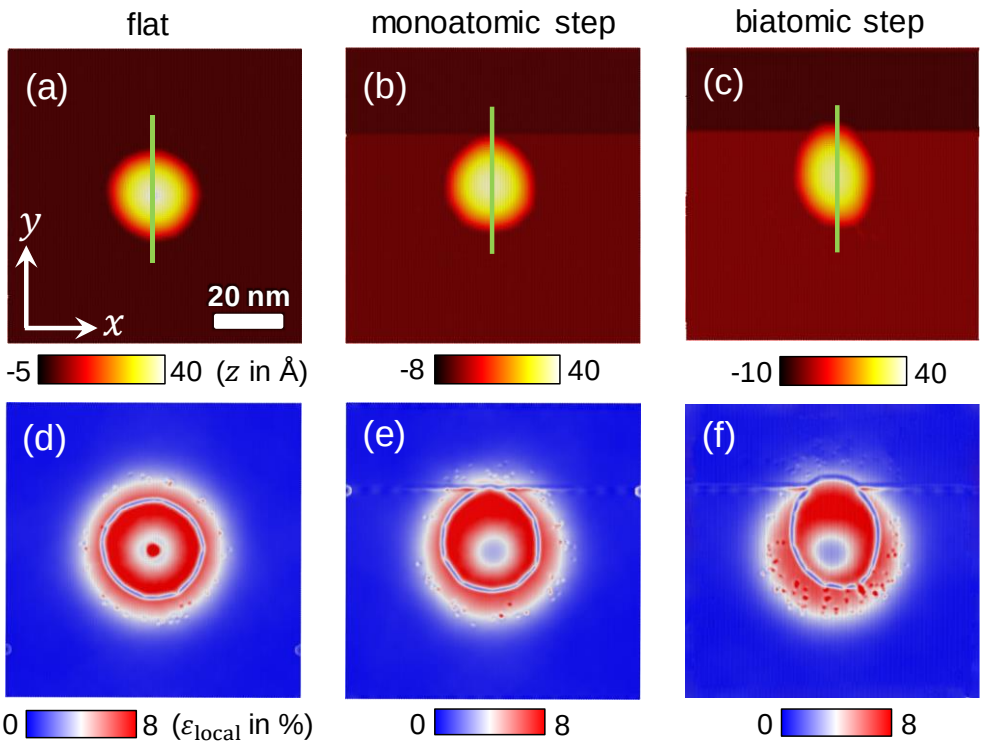

Figure S5. Topography and $\varepsilon_{\mathrm{local}}$ maps of relaxed MoS_2 membranes containing nanobubbles of $R \approx 17$ nm obtained in 100×100-nm^2 MD cells with perfectly flat Au (111) substrate (a, d); Au substrate with a monoatomic step (b, e); and Au substrate with a biatomic step (c, f).

S5. The Lennard-Jones potentials

The pair-wise 12-6 Lennard-Jones (LJ) model estimates the potential energy between two atoms separated by a distance r_{ij} through

$$V(r_{ij}) = 4\epsilon\left(\frac{\sigma^{12}}{{r_{ij}}^{12}} - \frac{\sigma^{6}}{{r_{ij}}^{6}}\right). \tag{S3}$$

Here, ϵ is the depth of the potential well and σ is the distance at which $V(r_{ij}) = 0$. The energy minimum of the potential well–satisfying $\mathrm{d}V(r_{ij})/\mathrm{d}r_{ij} = 0$–attains at a distance $r_0 = 2^{1/6}\sigma$. With $r_{ij} > r_0$, the potential energy smoothly vanishes towards 0, where the potential is strictly 0 after a cutoff radius [7].

We adopt the LJ values for both Mo-Mo and S-S interactions from Ref. [8]. The author in Ref. [8] which were used to reproduce DFT results of the elastic properties of monolayer MoS_2. The LJ coefficients for Au-Au and N-N interactions were taken from Refs. [9, 10], respectively.

In our MD simulations, we approximate the interaction energies between dissimilar atoms by means of the Waldman-Hadler mixing rules, which establish that the crossed LJ parameters between element 1 and element 2 follow

$$\sigma_{1-2} = \left(\frac{\sigma_1^6 + \sigma_2^6}{2}\right)^{\frac{1}{6}}, \tag{S4}$$

and

$$\varepsilon_{1-2}\sigma_{1-2}^6 = (\varepsilon_1\sigma_1^6\varepsilon_2\sigma_2^6)^{1/2}. \tag{S5}$$

It is important to mention that the above relations for mixed LJ parameters provide much better results than the widely used Lorentz-Berthelot rules, which may result in larger deviations from experimental data; see Ref. [11]. The LJ parameters used for the present simulations are given in Table S4.

Table S4. LJ coefficients used for the MoS_2/Au simulations.

LJ parameter	*N-N*	*Mo-N*	*S-N*	*Au-N*	*Au-S*	*Au-Mo*
σ (Å)	3.31	3.878	3.226	3.15	3.04	3.842
ϵ (meV)	3.214	1.084	6.581	10.501	22.818*	2.014*

*The MoS_2 bubbles discussed in the main text are those obtained in the simulations using $\epsilon = 3\epsilon^*$ for the Au-S and Au-Mo pairs, see the following Section S6 for further details about the role of ϵ in the resulting MD bubble profiles.

S6. The MoS_2/Au(111) coupling in the MD simulations

Van der Waals (vdW) forces fundamentally govern the relatively weak interlayer bonding between multilayer systems. We adopt the above LJ model to describe the vdW coupling between the MoS_2 layer and the Au(111) substrate (with the LJ parameters describing Au-Mo and Au-S interaction pairs given in Table S4). The LJ potential has been largely employed to prescribe the adhesion between single layers using MD simulations [12, 13, 14].

To assess the moiré patterns forming in flat MoS_2/Au(111) systems, we run complementary MD simulations that perform an NVT relaxation run over 100 ps. The results from these simulations show that the relaxed state of the heterosystem is characterized by a minimum interlayer spacing of $d \approx 2.85$ Å, see Fig. S6(b). Note that this value is slightly lower than that predicted from LJ pair-wise potential ($r_{0\,(S-Au)}$ = 3.412 Å). In addition, the moiré periodicity, h, observed in our MoS_2/Au(111) MD system (Fig. S6(c)) is in good agreement with experimental

observations [15], where $h \approx 3.3$ nm. Additionally, the resulting in-plane strain map from the moiré patterns of MoS_2 on Au(111) are given in Fig. S6(c, d), respectively.

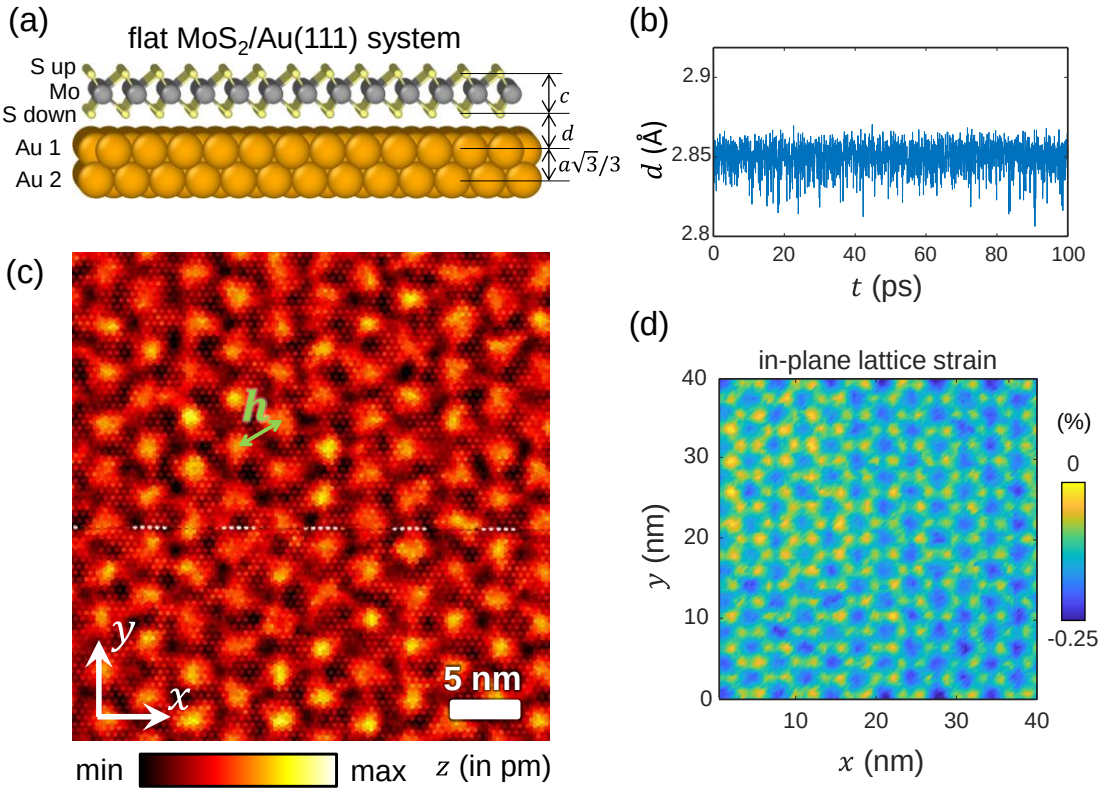

Figure S6. Relaxed MoS_2/Au(111) periodic system of size 40×40 nm using $\epsilon = 3\epsilon^*$. (a) Schematic representation of the MD cell. (b) Separation between flat MoS_2 and rigid Au (111), d, as a function of the relaxation time, t. (c) Moiré patterns in flat MoS_2/Au(111) predicted by MD. (d) Map of in-plane lattice strains. The in-plane strains are obtained from the computations of Mo-Mo bond distances using atom coordinates averaged over 5 ps.

S7. The role of the coupling with Au (111) in the MoS_2 bubble profiles

To investigate the role that the adhesion plays in the bubble topographies obtained in our MoS_2/Au(111) systems, we analyze the resulting shape of MoS_2 nanobubbles formed under distinct values of the LJ parameter ϵ from Eq.(S4). We define the ϵ values for Au-S and Au-Mo given in Table S4 as the reference values for the potential wells; hereafter referred as to ϵ^*= 23.2495 meV for Au-S and ϵ^*= 4.78038 meV for Au-Mo LJ interactions.

Following the semi-continuum formulation described by Zhu et al. [12], the cohesive energy between two flat layers, $\Phi_{\mathrm{m-s}}$, is defined in terms of the coupling LJ parameters and the corresponding area densities of the layers through the expression

$$\Phi_{\mathrm{m-s}} = 4\epsilon_{\mathrm{m-s}}\rho_{\mathrm{m}}\rho_{\mathrm{s}}\pi\left(\frac{\sigma_{\mathrm{m-s}}^{12}}{5d_{\mathrm{m-s}}^{10}} + \frac{\sigma_{\mathrm{m-s}}^{6}}{2d_{\mathrm{m-s}}^{4}}\right). \tag{S6}$$

Here, $\sigma_{\mathrm{m-s}}$ and $\epsilon_{\mathrm{m-s}}$ are the crossed LJ parameters between membrane (m) atoms and the substrate (s) atoms. $d_{\mathrm{m-s}}$ is the interlayer distance, whereas ρ_{m} and ρ_{s} are the area densities of the membrane and the substrate, respectively. Note that the MoS_2 membrane is composed of three layers of S up, Mo, and S down atoms (Fig.S6(a)) with a characteristic area density of $\rho_{\mathrm{m}} = 2/(3a_{\mathrm{m}}^2)$, and MoS_2 lattice parameters $a_0 = 3.19032$ Å and $c = 3.1298$ Å as predicated by the employed REBO potential [16]. A (111)-oriented FCC atomic layer is characterized by an area density of $\rho_{\mathrm{s}} = 4/(3\sqrt{2}a_{\mathrm{s}}^2)$, where the Au lattice parameter is $a_{\mathrm{s}} = 4.08$ Å [17].

In our (flat) MoS_2/Au(111) MD system, the total cohesive energy, Φ_{tot}, is then computed as the sum of all of the layer-by-layer contributions, namely

$$\Phi_{\mathrm{tot}} = \Phi_{\mathrm{S\ up-Au1}} + \Phi_{\mathrm{Mo-Au1}} + \Phi_{\mathrm{S\ down-Au1}} + \Phi_{\mathrm{S\ up-Au2}} + \Phi_{\mathrm{Mo-Au2}} + \Phi_{\mathrm{S\ down-Au2}}. \tag{S7}$$

Note in Eq. (S6) that the cohesive energy scales linearly with ϵ. This allows us to tune the vdW-type interactions between the MoS_2 and the Au substrate by simply varying the parameter ϵ. In this framework, we carry on several MD simulations under distinct values of ϵ (from $\epsilon = 1\epsilon^*$ to $\epsilon = 10\epsilon^*$) using 40×40- and 100×100-nm^2 MoS_2/Au(111) MD cells (Table S2) in order to assess the influence of the cohesive energy on MoS_2 bubble profiles.

Figures S7(a, b) show the resulting profiles of MoS_2 nanobubbles under varying values of parameter ϵ formed in 40×40- and 100×100-nm^2 cells, respectively. It is found that with increasing ϵ values, the larger cohesive energy between the MoS_2 and the substrate favors the formation of prominent nanobubbles characterized by a large h/R ratio, where $h/R = 0.35$ when $\epsilon = 10\epsilon^*$. The results from these simulations also suggest that the hydrostatic pressure measured inside relaxed MoS_2 nanobubbles markedly increases in prominent bubble profiles. For instance, a sixfold raise in P is observed in MoS_2 nanobubbles formed in 100×100-nm cells when the LJ coupling energy is increased tenfold (from $\epsilon = 1\epsilon^*$ to $\epsilon = 10\epsilon^*$). The same trends hold in the smaller bubbles from the 40×40-nm cells, where the h/R ratio varies from ≈0.075 ($\epsilon = 1\epsilon^*$) to ≈0.275 ($\epsilon = 10\epsilon^*$); see Figs. S7(c, d).

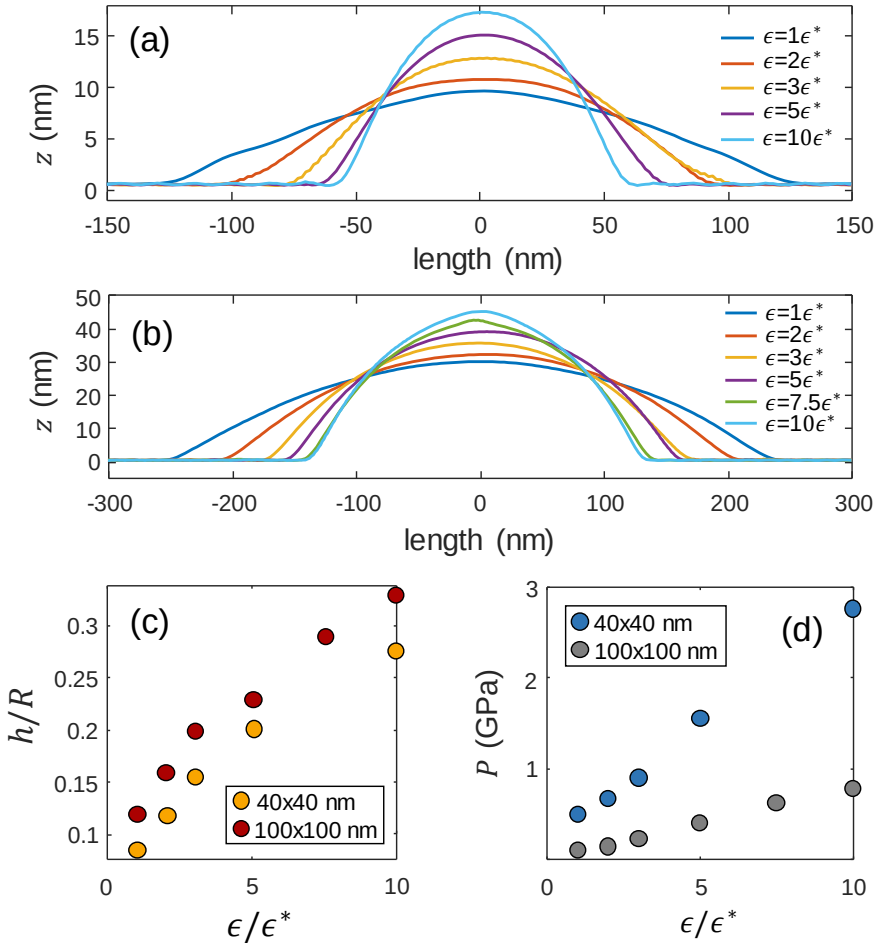

Figure S7. Properties of relaxed MoS_2 nanobubbles as a function of LJ parameter ϵ. (a, b): Bubble profiles formed in 40×40- and 100×100-nm, respectively. The evolution of the h/R ratio and the hydrostatic pressure with increasing LJ coupling is given in (c, d), respectively.

On the basis of our experimental results for MoS_2 bubbles with $R > R_c \approx 10$ nm (see Fig.1(d) in the main text)−which follow universal scaling in MoS_2/Au(111) systems with constant $h/R \approx 0.21$ (observation supported by other investigations; see, e.g, Ref. [18]), the analysis and discussion given in the main text feature simulations using the LJ values of $\epsilon = 3\epsilon^*$for the Au-Mo and Au-S interactions. Under these adhesion conditions, we estimate the cohesive energy between the MoS_2 and Au(111) substrate by means of Eqs. (S6, S7), and we obtain a value of $\Phi_{tot} \approx$ -335 mJ/m^2. This cohesive energy accounts for a 2D layer-substrate interaction with roughly similar adhesion levels to those measured in experiments of MoS_2 monolayers deposited on highly adhesive substrates [2].

S8. Computation of the hydrostatic pressure inside MD nanobubbles

The hydrostatic pressure inside the bubble, P, is related to the principal components of the 3-by-3 stress tensor, $\boldsymbol{\sigma}$, and the volume, V_{b}, of the trapped atoms through the equation [5]

$$P = -\left(\frac{\sigma_{11} + \sigma_{22} + \sigma_{33}}{3V_{\mathrm{b}}}\right). \tag{S8}$$

We systematically estimate V_{b} by means of the "Construct surface mesh" modifier featured in the OVITO visualization software [6]. The modifier constructs a surface representation of the instantaneous three-dimensional bubble shape composed of trapped atoms. It thus generates a geometric description of the outer and inner boundaries of the bubble in terms of a triangulated surface mesh, which allows for qualitative measurements of V_{b}.

S9. Computation of atomic-level strains in MoS_2 membranes

Atomic-level strain tensors in the top MoS_2 layers are calculated using the "atomic strain" modifier featured in OVITO. For the strain calculations, we assume plain strain in the MoS_2 membrane, where $\varepsilon_{xy} = \varepsilon_{yx}$ and $\varepsilon_{zz} = \varepsilon_{xz} = \varepsilon_{yz} = 0$. Then, the atomic Green-Lagrangian strain tensor is fully defined through

$$\mathbf{E} = \begin{pmatrix} \varepsilon_x & \varepsilon_{xy} \\ \varepsilon_{xy} & \varepsilon_y \end{pmatrix}. \tag{S9}$$

This algorithm allows us to obtain the strain tensor, **E**, at all the atomic sites in the MoS_2 membrane upon relaxation.

We calculate the local *intralayer* strains, $\varepsilon_{\mathrm{local}}$, via the squared sum of the eigenvalues of the strain tensor, **E**, [19]

$$\varepsilon_{\mathrm{local}} = \sqrt{\lambda_1^2 + \lambda_2^2} \qquad \text{with} \qquad \lambda_{1,2} = \mathrm{Eig}(\mathrm{E}). \tag{S10}$$

Alternatively, we also assess in the MoS_2 membranes the value of atomic-level maximum strains, $\varepsilon_{\mathrm{max}}$, whose analytical relationship with the components of tensor **E** from Eq.(S9)–assuming plain strain conditions–is fully defined by

$$\varepsilon_{\mathrm{max}} = \frac{\varepsilon_x + \varepsilon_y}{2} + \sqrt{\left(\frac{\varepsilon_x + \varepsilon_y}{2}\right)^2 + \left(\frac{\varepsilon_{xy}}{2}\right)^2}. \tag{S11}$$

Figure S8 shows the topography and the corresponding $\varepsilon_{\mathrm{local}}$ and $\varepsilon_{\mathrm{max}}$ maps of 15×15-nm (Fig. S8(a)) and 70×70-nm (Fig. S8(b)) MoS_2 membranes. To obtain an optimal definition in the strain maps of the MoS_2 membranes, the atomic-level deformations are computed taking an initial state (atom coordinates of unstrained, flat membranes) and the final relaxed MoS_2 membranes containing a nanobubble. We obtain the atom coordinates in the relaxed MoS_2 membranes using the final atom positions averaged over 5 ps. This leads to a smooth deformation field computed by means of the OVITO's modifier. The modifier cutoff value is set to 10 Å.

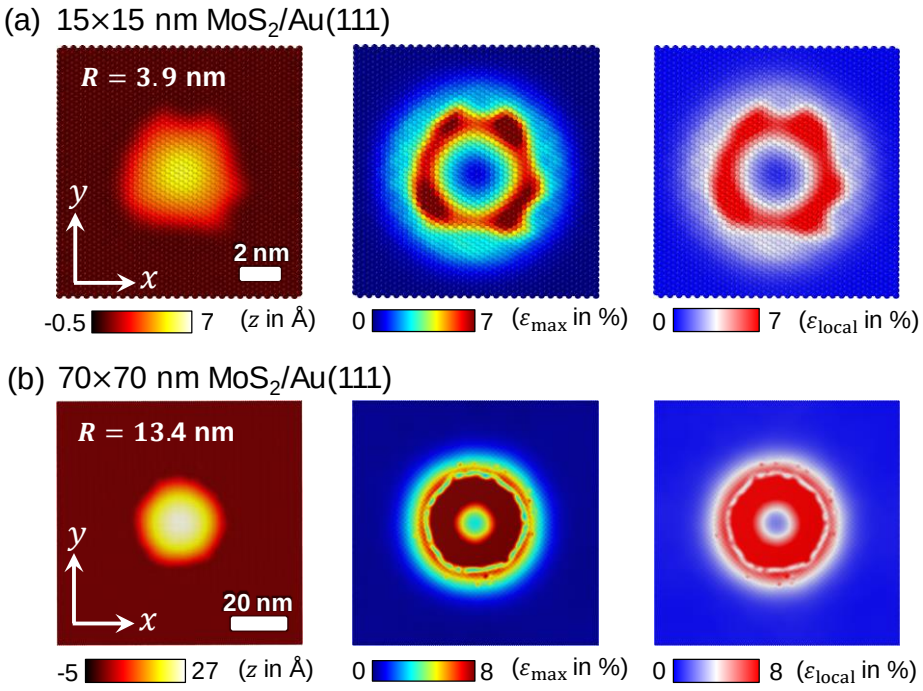

Figure S8. Topography and strain maps of relaxed, 15×15- and 70×70-nm^2 periodic MoS_2 membranes are given in (a, b), respectively.

S10. Strain states in MoS_2 nanobubbles

Further MD analyses of the atom-level strain components in the MoS_2 membranes unveil the development of a complex distribution of strain states during bubble the relaxation of MD bubbles. Figure S9 provides evidence of the attainment of a strain state in MoS_2 bubbles with a major biaxial contribution combined with uniaxial and shear states. A schematic of the strain states found in our

MD nanobubbles is provided in Fig. S9(b). We find that such a strain pattern develops irrespectively of the bubble's size (for the sake of brevity, we show in Fig. S9 only the results for R=6.7).

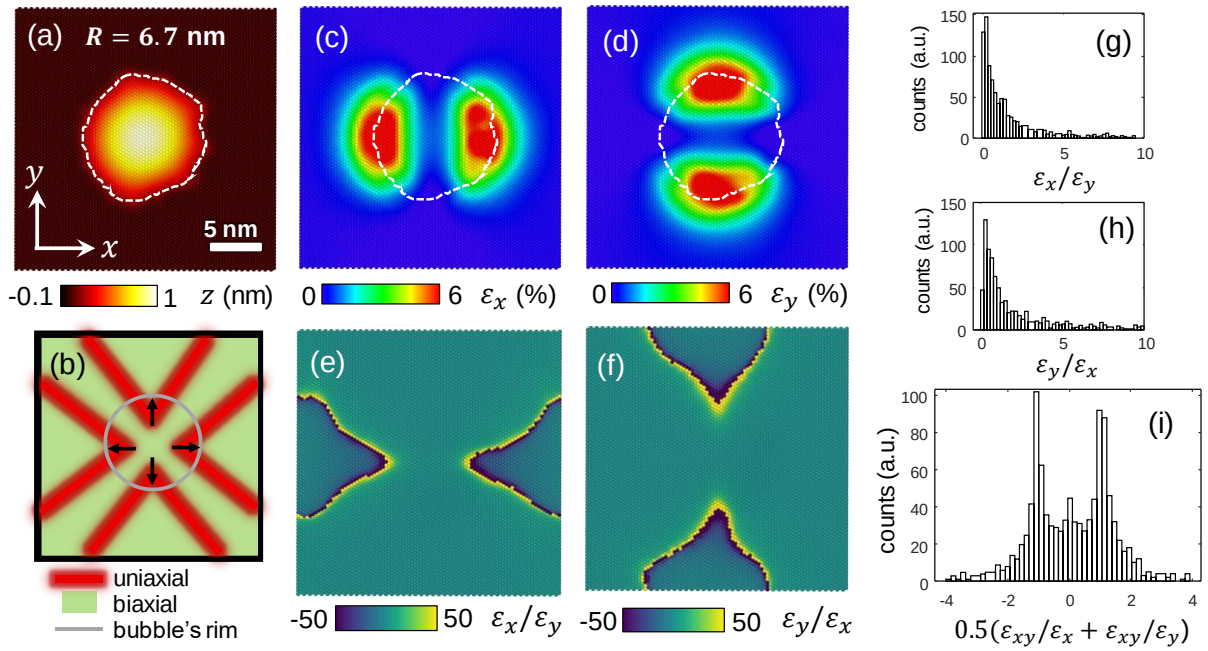

Figure S9. Strain states in relaxed 25×25-nm periodic MoS_2 membrane obtained from MD. (a) Topography map. (b) Schematic of the strain states found in our MD nanobubbles. The ε_x and ε_y maps of the membrane are given in (c, d), respectively. (e, f): $\varepsilon_x/\varepsilon_y$ and $\varepsilon_y/\varepsilon_x$ maps, respectively. Note in these maps that uniaxial states become manifest for $(\varepsilon_x/\varepsilon_y) \to \pm\infty$ and $(\varepsilon_y/\varepsilon_x) \to \pm\infty$. (g-i): Distribution of strain ratios inside the MD nanobubble, where bubble's edges are marked in (a, c, d).

S11. STM measurements of strain in MoS_2 nanobubbles

Resolving the atomic lattice in STM requires a sharp tip and a small tip-sample separation. Additionally, the number of points in the image must be sufficiently large to resolve the position of the atoms precisely, and the scan time must be sufficiently low to limit drift and distortions. A compromise is required, resulting in a limitation in the scanned area. Therefore, to measure the strain in MoS_2 nanobubbles as precisely as possible, in our STM experiments the lateral scan size was limited to ≈20 nm and the radii of the bubbles to ≈7 nm.

The strain, ε, was then measured by comparing the interatomic distance across the MoS_2 bubbles (d_{bubble}) to that measured on flat MoS_2 ($d_{\mathrm{MoS_2}}$) using the definition

$$\varepsilon = \frac{\Delta d}{d} = \frac{d_{\mathrm{bubble}} - d_{\mathrm{MoS_2}}}{d_{\mathrm{MoS_2}}}, \tag{S12}$$

expressed as a percentage (%).

To measure d_{bubble}, we acquired images of MoS_2 nanobubbles with atomic resolution (with the aforementioned limitations) and extracted their profiles in the radial direction. However, a few parallel profiles needed to be measured (Fig.S10(a)) in order to extract average measurements, thus departing from a truly radial direction. Additionally, to reduce the effect of drift, only the lattice direction nearest to the fast-scan direction was considered.

The atoms were identified as the peaks that modulate the bubble profiles (Fig.S10(b)). To ensure the correct identification of the positions of the peaks (i.e., the position of the atoms), a background was subtracted; see the blue line in Fig.S10(b). The distance between the atomic positions identified after this was defined as d_{bubble}. The background subtraction is especially important for the largest bubbles measured in this analysis, as these have heights of the order of the nm, which is 3 orders of magnitude larger than the height of the atomic protrusions (pm). The background was identified by means of a Gaussian function that approximates the expected profiles for bubbles in the bending-dominated regime [1].

Figure S10(c) shows the local ε values in various MoS_2 nanobubbles calculated using Eq. (S12). The error in our STM measurements of nanobubbles (≈10 pm) is notably larger than the error in the measurements of interatomic distances on nearly flat surfaces (such as the moiré-characterized regions of our samples), which is usually ≈1 pm. Although the procedure we employ to identify the position of the atoms in MoS_2 nanobubble profiles might contribute to the former error, we believe that the main contribution comes from tip-sample interactions on top of the bubbles. Most notably, the reduced interaction of MoS_2 with Au in the center of the bubble, which is pinned at the edge [2], allows for displacements of the MoS_2 membrane. Even though the tip was carefully prepared before each scan, the relatively high bias voltage (V_{bias} > 1 V) required to tunnel through MoS_2 in conjunction with the high current (I_{t} > 1 nA) needed for atomic resolution lead to an electric field that can locally deform the bubble's profile, displacing its atoms. Especially at room temperature, such tip-sample interactions are difficult to avoid. Additionally, lateral interactions of the tip on the curved surface of the bubble cannot be excluded. Even for small *z* displacements (of ≈1 Å), the interatomic distances between S atoms in the nanobubbles are of ≈3 Å so that the atomic forces acting on non-apex atoms of the tip are likely finite in magnitude.

However, the correspondence between the average strains measured by STM and those extracted from MD simulations (cf. Fig. 3(d) in the main text) suggests that such measurement errors are overall compensated along each bubble profile.

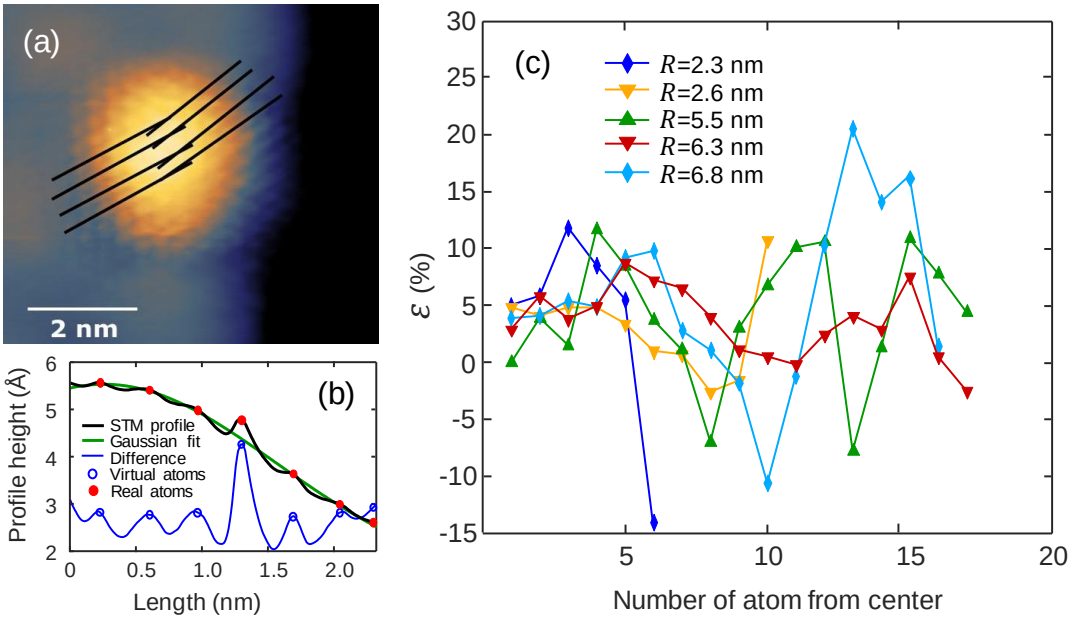

Figure S10. Strain measurement in MoS_2 nanobubbles. (a) STM topographic scan of a bubble with $R = 1.9$ nm. The black lines mark the profiles extracted for the strain measurements, spreading in radial direction from the center. (b) Measurement of the interatomic distance, d_{bubble}. The profiles marked in (a) are fitted by a Gaussian function (green line), which is used as background. Extracting the difference between the two curves (blue line) facilitates the identification of the in-plane position of the atoms (open blue circles). This is translated to the bubble profile (solid red circles) to measure the distances. (c) Local strains measured on 5 bubbles (averaged for various profiles). Note that the zero on the *x*-axis corresponds to the center of the bubble.

S12. STS spectra of MoS_2/Au(111)

The dI/dV spectra acquired on top of MoS_2 nanobubbles cannot be directly compared to those acquired on flat MoS_2 on the adjacent Au(111) terraces. This is because the contact with Au leads to a strong renormalization of the band structure of MoS_2 [21]. The hybridization of MoS_2 and Au(111) most clearly manifests as a finite dI/dV signal within the bandgap of MoS_2. The topographic scan of a MoS_2 nanobubble at the edge of an Au(111) terrace is displayed in Fig. S11(a). In this figure, the two crosses mark the position of the STS spectra given in Fig. S11(b),

as acquired on top of the bubble and on the terrace. Both spectra exhibit a bandgap. However, weak conduction is detected on the terrace. Additionally, the onsets of the valence and conduction bands appear broader because of the MoS_2-Au hybridization [21].

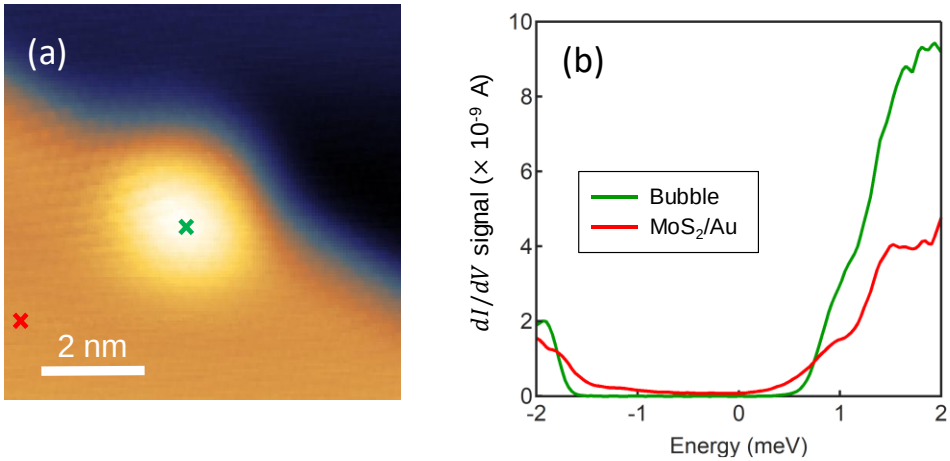

Figure S11. Comparison of STS spectra of MoS_2 on top of a bubble and on an Au terrace. (a) STM topographic scan of a bubble. The position of the spectra is marked by crosses. I_t = 0.5 nA, V_{bias} = 0.98 V. (b) Spectra on the bubble and on the terrace. Setpoint: I_t = 0.5 nA, V_{bias} = 0.98 V.

S13. Computation of the Raman spectrum of MoS_2 nanobubbles

The effect of strain on the Raman spectrum can be decomposed into its fundamental components; i.e., the frequency shift and the frequency splitting. Thus, the strain tensors computed in the MD MoS_2 bubbles (Section S8) are converted into Raman shifts of the $E^{(+)}$ (ω_E^+) and $E^{(-)}$ (ω_E^-) modes through the phonon shift rates, [22]

$$\Delta\omega_E^{\pm} = -\omega_E^0\,\gamma_E(\varepsilon_{xx}+\varepsilon_{yy}) \pm \frac{1}{2}\,-\omega_E^0\,\beta_E\sqrt{(\varepsilon_{xx}+\varepsilon_{yy})^2+4\varepsilon_{xy}^2}\ , \qquad \text{(S13)}$$

where ω_E^0 is the phonon frequency in the absence of strain (taken as 385.5 cm^{-1} for MoS_2), γ_E the Grüneisen parameter, and β_E the shear-strain phonon deformation potential. We adopt $\gamma_E = 1.1$ and $\beta_E = 0.78$, which were obtained in a 4-point bending (i.e., uniaxial deformation) experiment by Conley et al. [23].

The "Raman spectrum" is numerically simulated by calculating the $\Delta\omega_E^+$ and $\Delta\omega_E^-$ values (Eq. (S13)) for every Mo atom contained in the membrane area of interest. The individual Raman shift contributions are summed up by means of the full-width-at-half-maximum criterion [22]—set to 2 cm^{-1}—for each calculated individual peak. The overall normalized intensity distributions of

the simulated MoS_2 spectra are plotted in Figs. S12(a, b) for distinct areas. For comparison, the associated distribution of an unstrained MoS_2 membrane is also drawn in Fig. S12(a) with a dashed line.

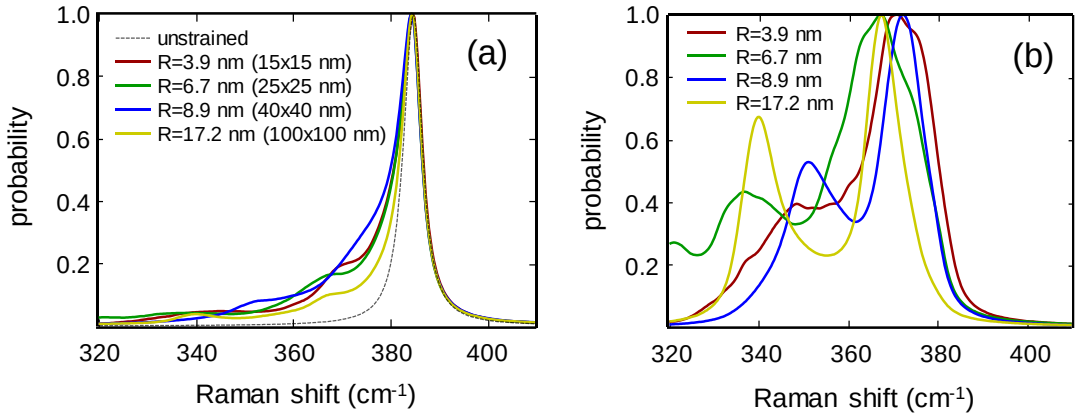

Figure S12. Simulated Raman spectra using MD analyses of the strain tensor, **E**. (a) Raman shifts of different MoS_2 periodic membranes containing a bubble (of radius R) at the center. (b) Raman shifts of different MoS_2 bubbles. Note in (b) that the Mo atoms used to compute the E-mode Raman shifts are those strictly contained in the MoS_2 bubbles.

References

[1] E. Khestanova, F. Guinea, L. Fumagalli, A. K. Geim and I. V. Grigorieva, "Universal shape and pressure inside bubbles appearing in van der Waals heterostructures," *Nature Communications,* vol. 7, p. 12587, 8 2016.

[2] D. Lloyd, X. Liu, N. Boddeti, L. Cantley, R. Long, M. L. Dunn and J. S. Bunch, "Adhesion, Stiffness, and Instability in Atomically Thin MoS2 Bubbles," *Nano Letters,* vol. 17, pp. 5329-5334, 2017.

[3] J. M. MacLeod, R. H. Miwa, G. P. Srivastava and A. B. McLean, "The electronic origin of contrast reversal in bias-dependent STM images of nanolines," *Surface Science,* vol. 576, pp. 116-122, 2005.

[4] S. Shabani, T. P. Darlington, C. Gordon, W. Wu, E. Yanev, J. Hone, X. Zhu, C. E. Dreyer, P. J. Schuck and A. N. Pasupathy, "Ultralocalized Optoelectronic Properties of Nanobubbles in 2D Semiconductors," *Nano Letters,* vol. 22, pp. 7401-7407, 2022.

[5] A. P. Thompson, S. J. Plimpton and W. Mattson, "General formulation of pressure and stress tensor for arbitrary many-body interaction potentials under periodic boundary conditions," *The Journal of Chemical Physics,* vol. 131, p. 154107, 2009.

[6] A. Stukowski, "Visualization and analysis of atomistic simulation data with OVITO–the Open Visualization Tool," *Model. Simul. Mat. Sci. Eng.,* vol. 18, p. 015012, 12 2009.

[7] M. P. Allen and D. J. Tildesley, Computer Simulation of Liquids, 2nd ed., O. U. Press, Ed., 2017.

[8] J. A. Stewart, "Atomistic Simulations of Defect Nucleation and Intralayer Fracture in Molybdenum Disulphide During Nanoindentation," 2012.

[9] Q. Pu, Y. Leng, X. Zhao and P. T. Cummings, "Molecular simulations of stretching gold nanowires in solvents," *Nanotechnology,* vol. 18, p. 424007, 2007.

[10] J. G. Powles and K. E. Gubbins, "The intermolecular potential for nitrogen," *Chemical Physics Letters,* vol. 38, pp. 405-406, 1976.

[11] C. Desgranges and J. Delhommelle, "Evaluation of the grand-canonical partition function using expanded Wang-Landau simulations. III. Impact of combining rules on mixtures properties.," *The Journal of chemical physics,* vol. 140, no. 10, p. 104109, 3 2014.

[,12] S. Zhu and T. Li, "Wrinkling instability of graphene on substrate-supported nanoparticles," *J. Appl. Mech,* vol. 81, 2 2014.

[13] L. Peng, H. Chan, P. Choo, T. W. Odom, S. K. R. S. Sankaranarayanan and X. Ma, "Creation of Single-Photon Emitters in WSe_2 Monolayers Using Nanometer-Sized Gold Tips.," *Nano Ltt.,* vol. 20, no. 8, pp. 5866-5872, 8 2020.

[14] Y. Guo and W. Guo, "Soliton-like thermophoresis of graphene wrinkles," *Nanoscale,* vol. 5, no. 1, pp. 318-323, 2013.

[15] C. C. Silva, D. Dombrowski, N. Atodiresei, W. Jolie, F. F. Hagen, J. Cai, P. T. P. Ryan, P. K. Thakur, V. Caciuc, S. Blügel, D. A. Duncan, T. Michely, T.-L. Lee and C. Busse, "Spatial variation of geometry, binding, and electronic properties in the moiré superstructure of MoS2 on Au(111)," *2D Materials,* vol. 9, p. 025003, 1 2022.

[16] T. Liang, S. R. Phillpot and S. B. Sinnott, "Parametrization of a reactive many-body potential for Mo--S systems," *Phys. Rev. B,* vol. 79, no. 24, p. 245110, 6 2009.

[17] X. W. Zhou, R. A. Johnson and H. N. G. Wadley, "Misfit-energy-increasing dislocations in vapor-deposited CoFe/NiFe multilayers," *Phys. Rev. B,* vol. 69, no. 14, p. 144113, 4 2004.

[18] J. Pető, G. Dobrik, G. Kukucska, P. Vancsó, A. A. Koós, J. Koltai, P. Nemes-Incze, C. Hwang and L. Tapasztó, "Moderate strain induced indirect bandgap and conduction electrons in MoS2 single layers," *npj 2D Materials and Applications,* vol. 3, p. 39, 10 2019.

[19] J. Quan, L. Linhart, M.-L. Lin, D. Lee, J. Zhu, C.-Y. Wang, W.-T. Hsu, J. Choi, J. Embley, C. Young, T. Taniguchi, K. Watanabe, C.-K. Shih, K. Lai, A. H. MacDonald, P.-H. Tan, F. Libisch and X. Li, "Phonon renormalization in reconstructed MoS2 moiré superlattices," *Nat. Mater.,* vol. 20, pp. 1100-1105, 8 2021.

[20] E. Blundo, T. Yildirim, G. Pettinari and A. Polimeni, "Experimental Adhesion Energy in van der Waals Crystals and Heterostructures from Atomically Thin Bubbles," *Phys. Rev. Lett.,* vol. 127, no. 4, p. 046101, 7 2021.

[21] A. Bruix, J. A. Miwa, N. Hauptmann, D. Wegner, S. Ulstrup, S. S. Grønborg, C. E. Sanders, M. Dendzik, Č. A. Grubi, M. Bianchi, J. V. Lauritsen, A. A. Khajetoorians, B. Hammer and P. Hofmann, "Single-layer MoS_2 on Au(111): Band gap renormalization and substrate interaction," *Phys. Rev. B,* vol. 93, no. 16, p. 165422, 4 2016.

[22] N. S. Mueller, S. Heeg, M. Peña-Alvarez, P. Kusch, S. Wasserroth, N. Clark, F. Schedin, J. Parthenios, K. Papagelis, C. Galiotis, M. Kalbac, A. Vijayaraghavan, U. Huebner, R. Gorbachev, O. Frank and S. Reich, "Evaluating Arbitrary Strain Configurations and Doping in Graphene with Raman Spectroscopy," *2D Mater.,* vol. 5, p. 015016, 2018.

[23] H. J. Conley, B. Wang, J. I. Ziegler, R. F. Haglund, S. T. Pantelides and K. I. Bolotin, "Bandgap Engineering of Strained Monolayer and Bilayer MoS 2," *Nano Letters,* vol. 13, pp. 3626-3630, 8 2013.